https://doi.org/10.1016/j.optlaseng.2020.106225

Optical nanoscale positioning measurement with a feature-based method

Chenyang Zhao [a, b], Chi Fai Cheung [b], Peng Xu [a, b*]

[a] School of Mechanical Engineering and Automation, Harbin Institute of Technology, Shenzhen 518055, China

[b] State Key Laboratory of Ultra-precision Machining Technology, Department of Industrial and Systems Engineering, The Hong Kong Polytechnic University, Hung Hom, Kowloon, Hong Kong, China

*** Corresponding Author.**
E-mail address: penghit.xu@connect.polyu.hk (P. Xu)

ABSTRACT: Traditional nanoscale positioning measurement methods require high-precision components and time-consuming calibration. To address these problems, this paper develops a fast and robust feature-based positioning (FRFP) method for optical nanoscale positioning measurement. Firstly, a unique polar microstructure surface is designed, and ultra-precision machined for imaging and matching. The next step uses the box filter which is computational saving to detect the initial feature points from the surface images. After that, the image scale is built to extract the robust feature points. The filter size is changed in each scale layer instead of image size to further reduce the number of calculations. Then, the orientation assignment process is conducted for angular displacement detection. After generating the robust feature points descriptors with 64-dimensional vectors, the feature point matching is performed to determine the absolute position changes between images. Finally, sub-pixel interpolation is also merged into the FRFP method to further improve the positioning resolution. To show the effectiveness of the FRFP method, experiments are conducted from the aspects of angular uncertainty, position uncertainty, measurement speed, and robustness respectively. All the experimental results demonstrate the efficiency and robustness of the FRFP method.

Keywords: Precision measurement, ultra-precision machining, microstructure surface

1 Introduction

Nanoscale positioning measurement is an important research area that has a significant influence on many other fields, such as manufacturing, optics, medical, and life science [1-3]. Currently, the common positioning measurement systems are mostly developed with laser interferometers, optical encoders, and so on [4]. Although laser interferometers are the most widely used equipment thanks to high precision, their calibration cost are high [5]. Since a linear encoder can only measure one single axis, the planar positioning measurement requires at least two sets of linear encoders. It not only increases the cost but also complicates the setup [6]. Moreover, the installation of measurement equipment is complex, and the related footprint area is also large.

The microstructure surfaces with small scale structures are applied widely due to their unique properties [7, 8]. Recently, the adoption of microstructure for precision positioning measurement is emerging. The technique is based on computer vision, integrating optoelectronics, and image processing technology to form a comprehensive measurement system. Compared with the conventional methods, this method can obtain the absolute position with the vision-based principle instead of laser scanning. However, most of these studies only focus on position measurement because the rotation measurement is difficult. Besides, another shortcoming of this method is its low measurement resolution. Although great achievements and significant contributions to solving the above problems have been done, it is worth noting that most studies use periodic patterns as the reference for positioning. It puts a high request on the manufacturing accuracy of the patterns and the calibration cost is also high.

Image processing algorithms are used in computer vision aim to improve stability, reduce hardware requirements, save costs, and increase efficiency during the detection of objects from their images [9]. A vision-based positioning method was proposed in Ref. [10], which creatively designed an anisotropic pattern named polar microstructure and used the image processing algorithms for absolute positioning. It was illustrated that this method could eliminate the calibration process and significantly reduce the cost [11]. Since a polar microstructure possessed a special pattern on the global surface [12], the template-matching (TM) method was subsequently used in the image processing. However, further investigation demonstrated that there were some limitations in the conventional TM method. Firstly, the calculation efficiency of TM may be one of the biggest obstacles for potential commercial applications [13]. Its exhaustive idea of finding the best matching position is very time-consuming. Secondly, the weak algorithm capabilities reduce the resistance to various external noise, such as machining error of microstructure surface, device assembly error, image scaling error, and environment error [14]. Thirdly, although the polar microstructure is designed considering its capability to detect the angular displacement, the conventional TM method is not suitable for angle detection. As a result, more advanced matching algorithms need to be presented.

Matching is a significant topic in image processing technology [15, 16]. Generally, there are two main matching categories including the intensity-based methods and the feature-based methods. The intensity-based methods compare the intensity patterns in images via correlation metrics [17]. While the feature-based methods can find correspondences between image features, such as points, lines, and contours [18-20]. The advantages of the feature-based methods lie in their high efficiency. For example, the Harris corner detector [21] is one of the classical detectors to extract corners and infer features of an image in the feature-based methods. Its significance not only lies in its efficient searching but also it is rotation invariant. It means that even if the image is rotated, it is still feasible to find the same corners as well as the rotation displacement. However, the operators in the Harris corner detector cannot detect the scale change because of simple illustrating. A corner may not be a corner if the image is scaled, which results in a failure in corner detection. To solve this problem, another classic algorithm scale-invariant feature transform (SIFT) was proposed [22] which extracted key points and computed its descriptors. Recently, a series of new generated algorithms have been established to increase the calculation speed, such as the features from accelerated segment test (FAST) [23], binary robust independent elementary features (BRIEF) [24], oriented FAST and rotated BRIEF (ORB) [25]. However, the abovementioned algorithms mostly focus on their applicability and fast response in different conditions. The resolution and its matching precision do not attract much interest.

Based on the above discussions, the demands of high resolution and measurement accuracy always motivate the algorithm development in the nanoscale positioning measurement. It is necessary to continuously improve the algorithm to realize the following objectives: (1) to measure the angle rotation displacement; (2) to speed up and improve the calculation efficiency; and (3) to enhance the robustness of the measurement system.

This paper proposed a highly advanced method that is suitable for optical nanoscale positioning measurement by taking account of both measurement requirements and calculation efficiency. The remainder of this paper is organized as follows. Section 2 presents the theory of algorithms in detail. A series of validation experiments are conducted to evaluate its measurement performance in Section 3.

Finally, the conclusion of this study is summarized in Section 4.

2 Fast and robust feature-based positioning method

Fig. 1 shows a specific surface with a polar microstructure for imaging [12], which is designed based on the concept of the polar coordinate system. The microstructure is fabricated followed a process chain of ultra-precision machining technology combining single point diamond turning (SPDT) and single point diamond broaching (SPDB). The designed microstructure possesses a unique pattern on the surface, which is specifically designed not only for the geometric patterns but also for the sorting of intensity values of pixels. The groove spacing for both circle and straight grooves are the same 50 μm. The grey-scale intensity distribution is unique which guarantees the reliability and the robustness. Although the surface roughness (Ra) of the microstructure is able to achieve about 10 nm, it should be pointed out that the surface quality has no influence on the measurement accuracy. It is because the proposed method is based on image matching and the polar microstructure only provides the non-periodic pattern. In fact, this is also one of the advantages of the proposed method.

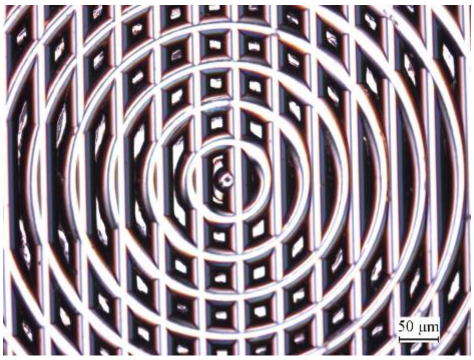

Fig. 1 Designed polar microstructure surface.

In this section, the algorithms of the fast and robust feature-based positioning (FRFP) method are described in detail as shown in Fig. 2, which can be divided into six steps, including: (1) feature point extraction; (2) building of the scale space; (3) feature point localization; (4) orientation assignment of feature points; (5) feature descriptor generation and (6) feature point matching. Each algorithm in the FRFP method is introduced in the following.

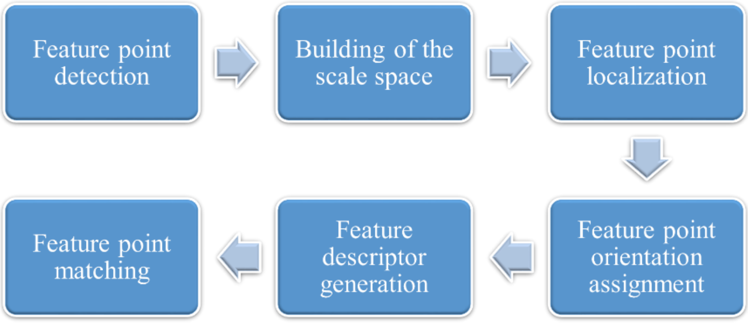

Fig. 2 Flowchart of the algorithms of FRFP method

2.1 Feature point detection

The purpose of feature point detection is to generate all interest points in the polar microstructure image by constructing a Hessian matrix. The Hessian matrix is a square matrix of second-order partial derivatives of a multivariate function that can describe the local curvature of the function. By generating stable edge points and blob points of an image, it can provide a basis for the feature detection.

For an image represented by $f(x, y)$, the Hessian matrix has the expression

$$H(f(x,y)) = \begin{bmatrix} \dfrac{\partial^2 f}{\partial x^2} & \dfrac{\partial^2 f}{\partial x \partial y} \\ \dfrac{\partial^2 f}{\partial x \partial y} & \dfrac{\partial^2 f}{\partial y^2} \end{bmatrix} \tag{1}$$

where x, y represents a location of a point.

Normally, the Gaussian filtering of the image is required before constructing the Hessian matrix. The filtered Hessian matrix by Gaussian filtering in $f(x, y)$ at scale σ can be expressed as

$$H(f,\sigma) = \begin{bmatrix} L_{xx}(f,\sigma) & L_{xy}(f,\sigma) \\ L_{xy}(f,\sigma) & L_{yy}(f,\sigma) \end{bmatrix} \tag{2}$$

where L_{xy}, L_{xy} and L_{yy} represent the convolution of the Gaussian second-order partial derivative in the x, y and coupled xy direction, respectively.

To increase the operation speed, the Gaussian filter is replaced by the box filter. The relation of the Gaussian filter template and a box filter template is shown in Fig. 3. Fig. 3(a) and Fig. 3(b) illustrate the 9×9 Gaussian filter template in the y and xy direction, respectively. To reduce the calculation cost, L_{yy} and L_{xy} in the Gaussian filter template are approximated to be D_{yy} and D_{xy} in the box filter template as depicted in Fig. 3(c) and Fig. 3(d). Specifically, L_{yy} is changed to D_{yy} by enabling that the gray part has a uniform pixel value of 0, the black part is -2, and the white part is 1, respectively. This approximate approach helps to use the concept of integral images in the next step, which can significantly reduce the number of calculations.

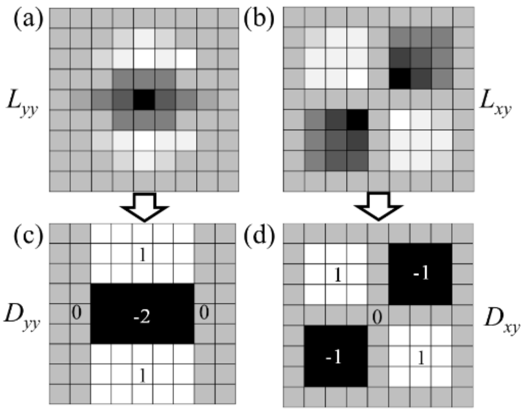

Fig. 3 Evolution from the Gaussian filter to the box filter: (a) Gaussian filter template in *y* direction, (b) Gaussian filter template in *xy* direction, (c) box filter template in *y* direction, and (d) box filter template in *xy* direction.

The box filter can increase the calculation speed by using the integral images for image convolution. As shown in Fig. 4, the main idea of the integral image is to store the sum of the pixels of a rectangular area formed by the image from the starting point to each point as an element of an array. When calculating the pixels of a specific area, the elements of the array can be directly indexed. The sum of the pixels in this area is recalculated, which speeds up the calculation. As shown in Fig. 4, the cumulative pixel value of any point $f(x, y)$ in the integral image is the sum of the pixel intensity values of the corresponding focus area from the upper left corner of the original image to the arbitrary point $f(x, y)$. The mathematical formula is expressed as

$$P(x, y) = \sum_{i' \le x,\, j' \le y,} p(i, j) \tag{3}$$

where $P(x, y)$ represents the cumulative pixel grey value of any point $p(i, j)$.

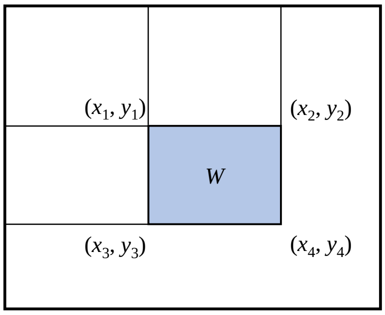

Fig. 4 Concept of integral images.

The filtering of the image by the box filter is translated into the calculation of the addition and subtraction of the pixel sums between different regions on the image. The calculation can be accomplished simply by looking up the integral graph several times. Once the integral of a region of an image is determined, it only needs to calculate the area value of *W* as shown in Fig. 4. The mathematical expression is

$$\sum_W = P(x_4, y_4) - P(x_2, y_2) - P(x_3, y_3) + P(x_1, y_1) \tag{4}$$

When the determinant of the Hessian matrix has a local maximum, it can be determined that the current point is a brighter or darker point than other surrounding points. With this method, the position of the key point is located. The determinant of the Hessian matrix can be expressed as

$$\begin{aligned}
\mathrm{Det}(H) &= L_{xx}L_{yy} - L_{xy}L_{xy} \\
&= D_{xx}\frac{L_{xx}}{D_{xx}}D_{yy}\frac{L_{yy}}{D_{yy}} - D_{xy}\frac{L_{xy}}{D_{xy}}D_{xy}\frac{L_{xy}}{D_{xy}} \\
&= D_{xx}D_{yy}\left(\frac{L_{xx}}{D_{xx}}\frac{L_{yy}}{D_{yy}}\right) - D_{xy}D_{xy}\left(\frac{L_{xy}}{D_{xy}}\frac{L_{xy}}{D_{xy}}\right) \\
&= \left(D_{xx}D_{yy} - D_{xy}D_{xy}\left(\frac{L_{xy}}{D_{xy}}\frac{L_{xy}}{D_{xy}}\right)\left(\frac{D_{xx}}{L_{xx}}\frac{D_{yy}}{L_{yy}}\right)\right)\left(\frac{L_{xx}}{D_{xx}}\frac{L_{yy}}{D_{yy}}\right) \\
&= (D_{xx}D_{yy} - (\omega D_{xy})^2)C
\end{aligned} \tag{5}$$

where ω is the relative weight of the filter responses, C is a constant that does not affect the comparison of extreme points.

As shown in Fig. 3, the 9 × 9 box filters are approximations of a Gaussian with $\sigma = 1.2$. Then, ω in Eq. (5) can be expressed as

$$\omega = \frac{|L_{xy}(1.2)|_{\mathrm{F}}\, |D_{xy}(9)|_{\mathrm{F}}}{|L_{xx}(1.2)|_{\mathrm{F}}\, |D_{xy}(9)|_{\mathrm{F}}} = 0.912 \tag{6}$$

where $\|\cdot\|$ represents the Frobenius norm.

Thus, Eq. (5) can be simplified as

$$\mathrm{Det}(H) = D_{xx}D_{yy} - (0.912D_{xy})^2 \tag{7}$$

The weighting factor 0.912 is multiplied by D_{xy} to balance the error due to the use of box filter approximation. In addition, the response value is also normalized according to the filter size. The approximate Hessian matrix determinant is used to represent the blob response value at a certain point in the image. All the pixel points in the image are traversed to form a response image of all points detected at a certain scale. Using different template sizes, a multi-scale blob response map is formed, which is used in feature point localization in the polar microstructure image.

2.2 Building of the scale space

Image scale change is a very challenging problem especially for the precision positioning, and the image scale directly determines the actual pixel size. Hence, the feature points need to have scale invariance property and calculations at multiple scales are required. A common way of multi-scale computation is to build the image pyramid, as shown in Fig. 5(a). The filter is unchanged, but the same image is down-sampled at different scales. The smaller-scale image is in the upper layer in the pyramid. Most algorithms, such as SIFT, use the same way to build up the scale space as shown in Fig. 5(a). However, each down-sampled image requires a lot of calculations costs. In order to take advantage of the box filter and the integral image, the proposed FRFP method uses an algorithm that does not change the image size, as shown in Fig. 5(b). Alternatively, the size of the filter core is changed in each scale layer. For each sampling process, the calculation amount of changing box filter size is much smaller than adjusting the image size. This method ensures a further increase in calculation speed.

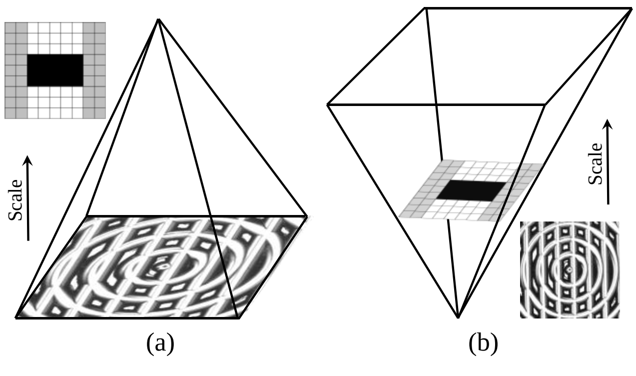

Fig. 5 Scale pyramid of polar microstructure surface in (a) SIFT method, and (b) FRFP method.

Since this algorithm is used in precision positioning, the environment has very low distortion and scale change. To reduce the calculation amount and further increase the measurement speed, the proposed algorithms shorten the scale of the space so as to reduce the number of octaves and intervals.

2.3 Feature point localization

To locate the feature points in different images with different sizes, a 3×3×3 neighbourhood non-maximum suppression method [26] is adopted. The main idea is that all values less than the present detection threshold can be discarded. It should be noticed that the number of detected feature points mainly depends on the threshold. For the precision positioning measurement, the detection threshold should not be too large on the condition that the number of detected feature points is enough. It ensures that the position of the identified feature point is accurate with high matching accuracy. In this study, the number of feature points keeps being in the range of 20 to 40 per image.

A box filter corresponding to the image resolution of the scale layer is used for detection. As shown in Fig. 6, a 3×3 filter is taken as an example. One of the nine-pixel points in the same scale layer image is used to detect the feature point. After that, it compares with the rest eight points on the same scale layer, followed by the nine points on the top and bottom of the two-scale layers. Hence, there are points 26 points in total. If the feature value of the pixel is larger than the surrounding pixels, the point can be determined as the feature point.

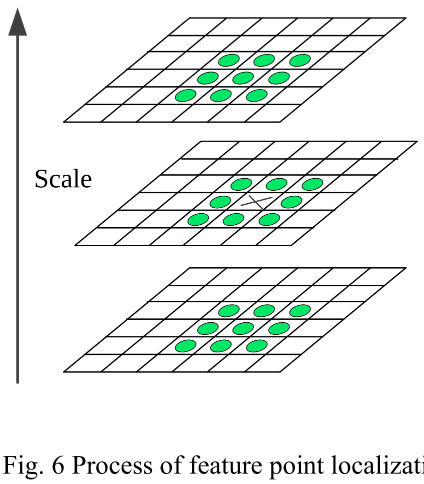

Fig. 6 Process of feature point localization.

2.4 Feature point orientation assignment

In this algorithm, the feature of the Haar wavelet in the circular neighborhood of statistical feature points is used [27]. Within the circular neighborhood of the feature points, the feature sums of horizontal and vertical Haar wavelet of all points within a 60° sector area are counted. Considering the detection resolution of angular displacement, the angular resolution is set to be 0.01° in order to improve the accuracy of the angular displacement detection. The Haar wavelet eigenvalues within the region are counted again as shown in Fig. 7. The direction of the sector with the most significant value is regarded as the main orientation of this feature point.

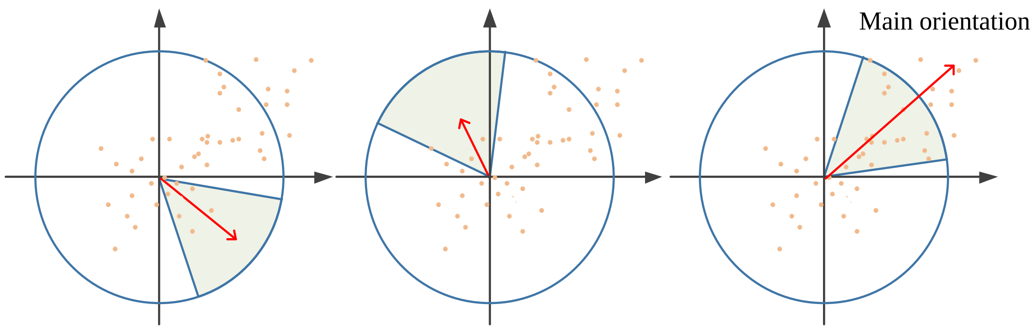

Fig. 7 Orientation assignment of the feature points.

2.5 Feature descriptor generation

The feature descriptor is an essential indicator to describe the information stored in each feature point of the polar microstructure image. In order to generate the descriptor, a square area with 4×4 sub-region grids is also taken around the feature point as shown in Fig. 8. The direction of the obtained square area is along the main direction of the feature point. Each sub-region counts the horizontal and vertical Haar wavelet, where the horizontal direction is denoted as dx and the vertical direction is denoted as dy. The abovementioned directions are relative to the main orientation. To improve the robustness against the noises such as localization errors, deformation and distortion, the algorithm firstly makes dx and dy weighted with a Gaussian function ($\sigma = 3.3$) centered on the feature point.

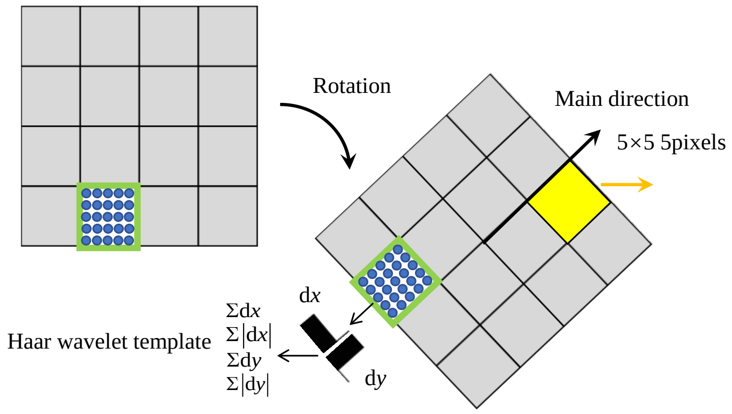

Fig. 8 Generation of feature point descriptors.

In each sub-region, the Harr wavelet response of 25 pixels is calculated. It should be noticed that the Haar wavelet response has four parameters, including the absolute values, which are calculated to obtain information about the polarity of the changes of pixel intensity. Then, the feature vector $\boldsymbol{v}$ in each sub-region can be expressed as

$$\boldsymbol{v} = \left(\sum \mathrm{d}x, \sum \mathrm{d}y, \sum |\mathrm{d}x|, \sum |\mathrm{d}y|\right) \tag{8}$$

where $\sum \mathrm{d}x$ is the sum of horizontal direction value, $\sum \mathrm{d}y$ is the sum of vertical direction value, $\sum |\mathrm{d}x|$ is the sum of horizontal absolute value, and $\sum |\mathrm{d}y|$ is the sum of the vertical absolute value.

Taking these four values as feature vectors for each sub-block region, a total of 64-dimensional vectors is used as descriptors for the feature points, which guarantees the richness of information. Finally, in the surrounding region area of each feature point, there is a feature descriptor vector whose length is 64.

2.6 Feature point matching

After obtaining the feature descriptor, the matching between feature points in two images is the final objective. Similar to SIFT, the proposed method determines the matching degree by calculating the Euclidean distance [28] between two feature points. The shorter the Euclidean distance, the better the matching degree that represents the two feature points. The difference is that the proposed method adds the judgment of the Hessian matrix trace. If the sign of the matrix traces of the two feature points is the same, it means that the two features have a contrast change in the same direction. If they are different, the contrast between the two feature points is shown. The direction of change is reversed, even if the

Euclidean distance is 0, and it is also excluded directly.

To improve the matching resolution, FRFP adds the sub-pixel interpolation algorithm into the section of feature point matching. It should be noticed that the sub-pixel interpolation is conducted after determining the best-matched original pixel to improve the calculation speed. In this study, the bilinear interpolation (BI) algorithm [29] is chosen to be the pixel interpolation algorithm in FRFP. After BI step, each previous pixel is divided into smaller pixels with a higher resolution. The theoretical resolution improves from 1 pixel to $1/(k_{Inter}+1)$ pixel, where k_{Inter} refers to the number of interpolation points in a single pixel. Therefore, a higher measurement accuracy is realized by second stage FRFP matching in the sub-pixel level.

3 Experimental verification

To demonstrate the application and effectiveness of the proposed FRFP method, experiments were conducted, and the results were compared with the conventional TM method. Four aspects of improvements were addressed including angular measurement uncertainty, position measurement uncertainty, measurement speed, and robustness.

3.1 Angular measurement uncertainty

Besides the orientation detection function in the FRFP method, the design of the polar microstructure also contains feature lines that are easy to be detected. However, due to the complicated practical condition, it may involve some noises and changes. To show the angular displacement measurement under real conditions with the FRFP method, an experiment was conducted on an ultra-precision diamond machining machine tool (Moore Nanotech 350FG, USA) as shown in Fig. 9. There are totally four axes in the machine tool, including three linear axes (X, Y, Z) and a rotational axis (C). The rotational axis is used as the main axis owing to its high accuracy and repeatability. It has a feedback resolution with 0.01 arc seconds and a rotational accuracy of ±1 arc seconds (compensated). As shown in Fig. 9, a polar microstructure surface was mounted on the vacuum chuck together with its fixture. A CCD microscope (Optem M Plan APO 20x) installed on the drive stage was used to measure the surface of the polar microstructure. The angular displacement was detected by comparing the measured images at different rotation statuses.

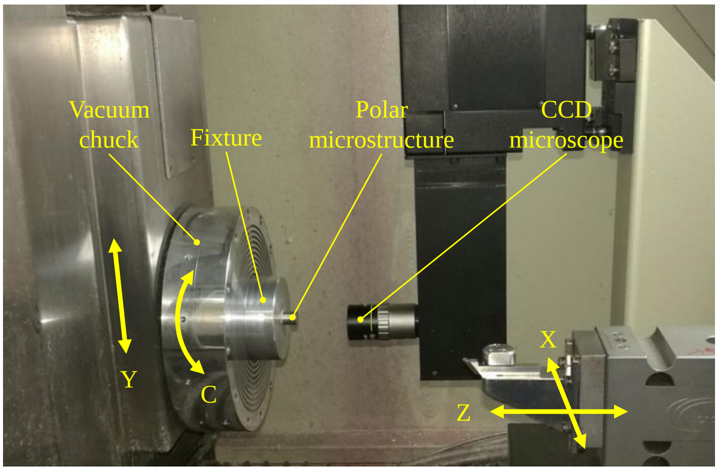

Fig. 9 Experimental setup for the angular displacement measurement.

As an example, Fig. 10 shows the calculation process of the angular displacement. Initially, the pose of the microstructure surface is shown in Fig. 10(a). After rotating 10° clockwise, the pose of the microstructure is shown in Fig. 10(b). To compare the two images, they are superimposed together as illustrated in Fig. 10(c), where the feature points were detected, extracted and marked with red points. The feature point descriptor algorithm was then used to find the possible matched feature point pairs, and each feature point pair was connected by a straight line as shown in Fig. 10(c). Finally, the two images were matched by the detected feature point pair as shown in Fig. 10(d), where the original image in Fig. 10(a) was at the bottom and the original image in Fig. 10(b) was at the upper layer. The difference of the two layers was shaded green to clearly show the angular displacement of the two images. Once the localization and orientation assignment of feature points are obtained, the accurate angular displacement can be determined according to the above data. This is a single process for angular displacement measurement using the FRFP method.

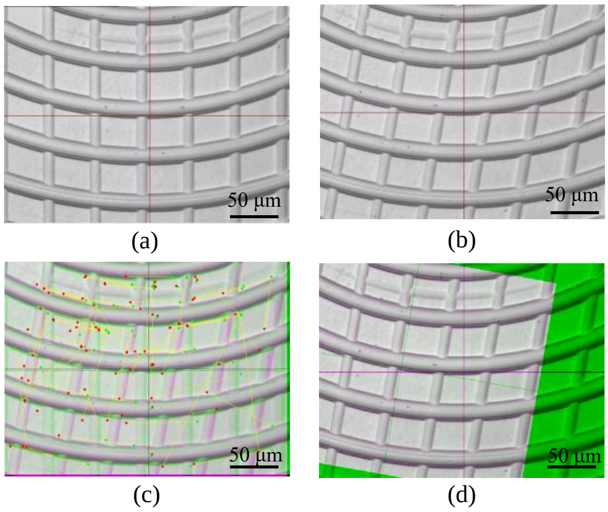

Fig. 10 Calculation process of the angular displacement: (a) initial pose; (b) 10° rotated pose; (c) feature points detection; and (d) matching result.

When the feature points are detected, the orientation of the images can be determined. To test the angular measurement uncertainty of the FRFP algorithm, a set of experiments was conducted every 60° when the C-axis rotated from 60° to 360°. The experiments were repeated five times, which means C-axis was rotated 30 times from the initial pose. In each pose, the polar microstructure was captured with the CCD microscope and the image was stored in the database. The captured images were processed with the FRFP method to output the angular displacement at each pose. Meanwhile, the actual absolute angular displacements of the C-axis shown on the machine were recorded. As depicted in Fig. 11, the bar chart illustrates the output results of angular displacements calculated by the FRFP method, while the line graph represents the measurement uncertainty (calculation error).

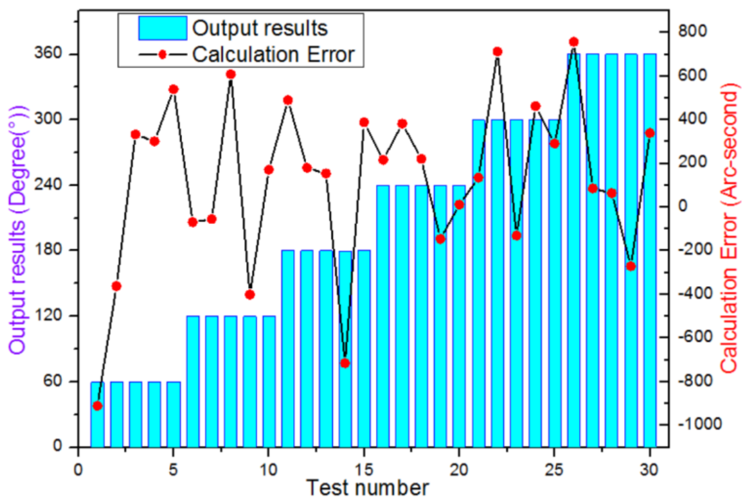

Fig. 11 Measurement uncertainty of angular displacement.

Compared with the C-axis data recorded from the machine tool. In the algorithm, the resolution of angle measurement is set as 36 arc-second (0.01°). It can be found that among the 30 measurements, the angular measurement uncertainty is within the range of ± 800 arc-seconds. Most uncertainty values are centralized in the interval between -200 and 400 arc-seconds. The average value of the uncertainty is 126.44 arc-seconds, and the corresponding standard deviation is 388.64 arc-seconds. The results indicate that the FRFP method can achieve 100-arcsecond level angular measurement uncertainty.

3.2 Positioning measurement uncertainty

To test the measurement uncertainty of position displacement using the more accurate instrument instead of machine tool, the experiment was conducted on a coordinate-measuring machine (CMM) (Video-Check UA 400 3D CNC, Werth Inc., Germany) as shown in Fig. 12. This CMM possesses 1 nm level resolution and 0.15 μm uncertainty of position displacement measurement. It is equipped with a CCD microscope with a resolution of 1356 × 1021 pixels, where one pixel is 454.20 nm in the X-direction and 453.76 nm in the Y-direction. In the experiment, the polar microstructure workpiece was placed on the platform of the CMM, and the CCD microscope measured the polar microstructure surface vertically.

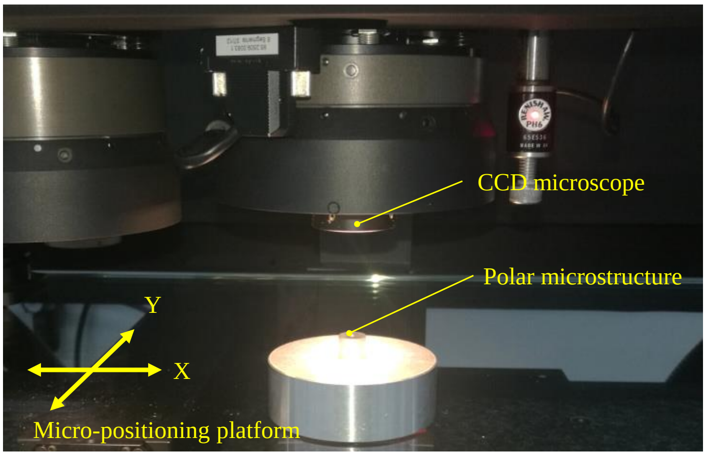

Fig. 12 Experimental setup for the position displacement measurement.

During the uncertainty measurement, the micro-positioning stage of the CMM was driven as shown in Fig. 13 to reduce the errors from CMM along the two directions (X and Y-axis). The total measurement range is 200 μm. The drive stage of the CMM moves along the X-axis in 20 μm steps from the starting point 0 μm to 200 μm as shown in Fig. 13(a). After that, the drive stage moves back to the next row and repeats the abovementioned motions until it is moved to the endpoint as shown in Fig. 13(a). The solid arrow represents the X direction movement and the dotted arrow represents movement in the Y direction. The experimental step to test the measurement uncertainty along the Y-axis is shown in Fig. 13(b), whose motion locus is just reversed from the previous X-axis.

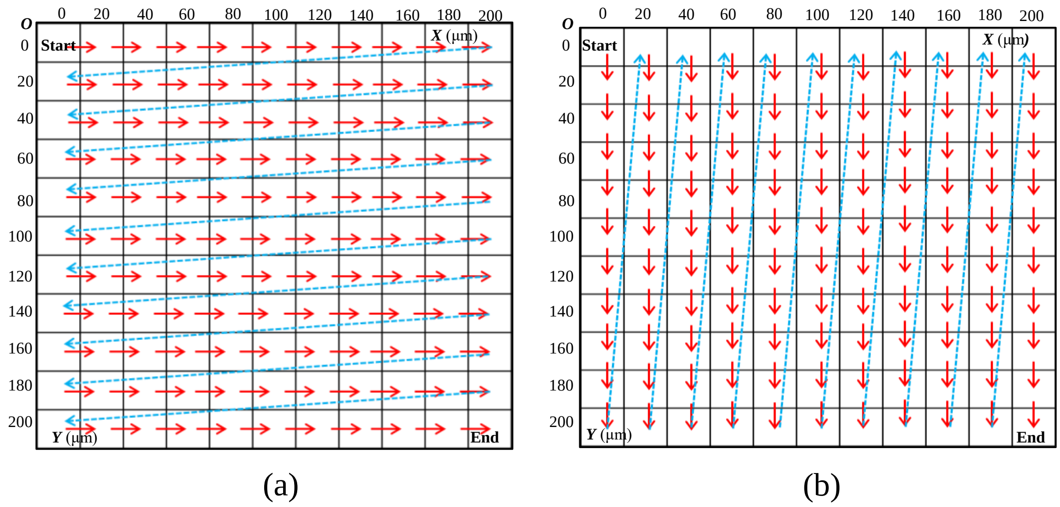

Fig. 13 Measurement locus of the position displacement measurement uncertainty test: (a) X-axis uncertainty test, and (b) Y-axis uncertainty test.

For the X-axis uncertainty test, every 10 measured points were chosen as one group with a constant X-axis value, but Y-axis values vary from 20 μm to 200 μm. A total of 10 groups containing 100 measured points were selected and their X-axis values were calculated by the FRFP method. The same approach was performed for the Y-axis. After obtaining the data from the total 200 measurement points in two axes, the results illustrate that the average value of position displacement measurement uncertainty on the X-axis is 2.1 nm and its standard deviation value is 44.62 nm. On the Y-axis, the average value of position displacement measurement uncertainty is -4.45 nm and its standard deviation value is 43.31 nm. To give a comparison with the TM method, Table 1 summarizes these parameters of the two methods. From the table, it can be concluded that the FRFP method is superior to TM method from the view of position displacement measurement uncertainty on the two motion axes.

Table 1 Position displacement measurement uncertainty performance comparison between the two algorithms

Parameters	TM	FRFP
Length range of measurement	100 μm	200 μm
Step distance of measurement	10 μm	20 μm
Number of measured points	200	200
Average of X-axis uncertainty	109.6 nm	2.1 nm
Average of Y-axis uncertainty	91.8 nm	-4.5 nm
Standard deviation of X-axis uncertainty	76.4 nm	44.6 nm
Standard deviation of Y-axis uncertainty	69.7 nm	43.3 nm
Parameters	TM	FRFP

3.3 Measurement speed

In this experiment, the measurement speed of the FRFP method is evaluated. Since one of the most significant features of the FRFP method is its fast calculation speed, the actual performance should be tested and compared with the TM method. In the TM method, the position is obtained through a template image and a global image. The calculation amount is mainly determined by the pixel size of the template image and the global image. While in the FRFP method, the calculation amount is much less influenced by the pixel size. To validate the analysis and control variables, this experiment was divided into two parts. The first part was conducted when the pixel size of the global image was a variable and that of the template image was fixed. The condition diagram is shown in Fig. 14(a). The other was the reversed condition where the pixel size of the template image was the variable and that of the global image was fixed as shown in Fig. 14(b).

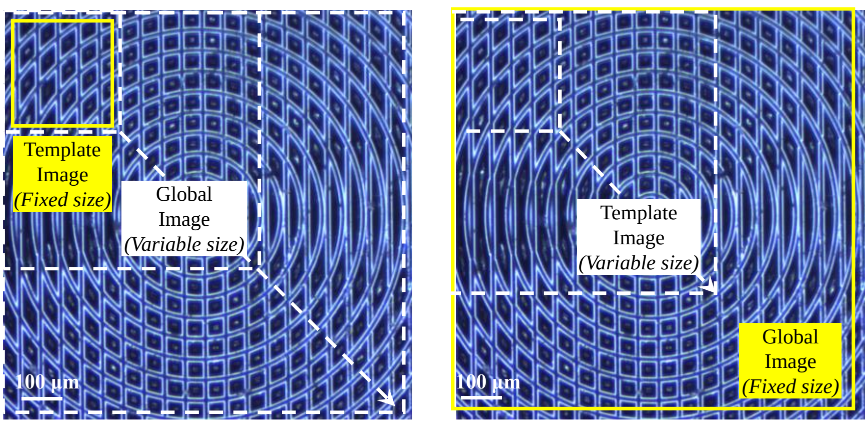

(a) (b)

Fig. 14 Experimental diagrams: (a) fixed-size template image and global image with variable size, and (b) fixed-size global image and template image with variable size.

In Fig. 14(a), the template image remained the same in the whole experiment, but the size of the global image increased from the upper left corner (500-pixel size) to the bottom right corner (1944-pixel size). Each step increased one pixel. Meanwhile, the two images were used in the FRFP method to ensure the consistency of the experimental conditions. The whole experiment was conducted using the software Matlab 2018b on the same computer with the processor Intel (R) Core (TM) i7-6600U CPU. After each calculation, the consumed time was recorded automatically by the program.

The experimental results were shown in Fig. 15. The ball-shaped scatter plot denoted the calculating time of each image pair in the TM method while the diamond-shaped scatter plot represented that of the FRFP method. To clearly show the comparison of the two methods, the ordinates were expressed in the log form. It can be found that when the global image size ranged from 500 to 800, the calculation time for the TM method was relatively stable, around the 10 s level. However, when the global image size was larger than 900, the calculation time surged constantly. It required nearly 10000 s with the largest size at 1944 pixels. The huge calculation amount for the TM method is the decisive reason when the size of the global image increases. For the FRFP method, its calculation time slowly increased from 0.2 s to 0.5 s, and the average of consuming time was 0.38 s. Although the accuracy of timing control is not precise, the gap between TM method and the FRFP method is surprising, especially when the image pixel is large.

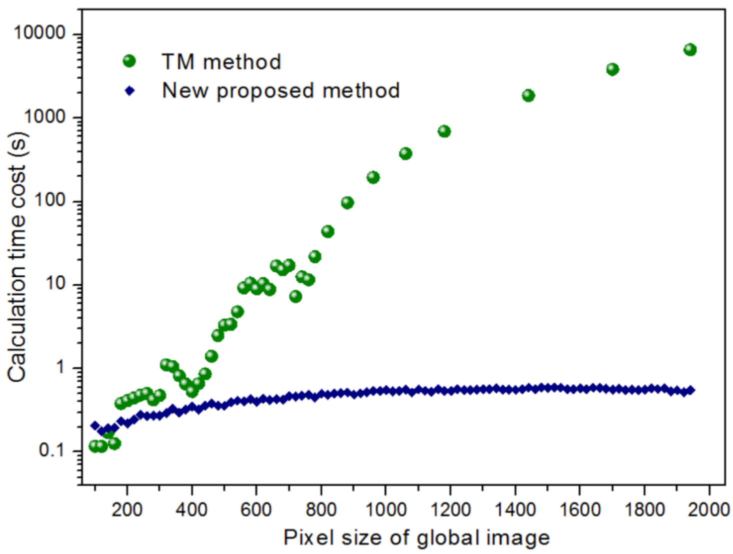

Fig. 15 Comparison between two algorithms in the case where the template image size is fixed.

Similarly, a contrast experiment was also conducted as shown in Fig. 14(b). Compared with the previous test, the difference was that the global image size was fixed while the template image size varied from 200 to 1940. The experimental results were shown in Fig. 16. It was interesting to note that the calculation times for the TM method reached the maximum when the template image size was in the middle range. The overall trend exhibited a parabolic form. For the FRFP method, its calculation time increased a little as compared with the previous experimental results. The average consuming time was 0.86 s. The reason was that one image size (template image size) for the previous experiment was fixed at 200 pixels. While in this experiment, one image size (global image size) was fixed at 1944 pixels. It indicated that the pixel size also influenced the calculation time of the FRFP method. However, the improvement in calculation speed was significant for the FRFP method.

From the theoretical analysis, with the increase of pixels, the calculation amount of the TM method grows exponentially but it grows approximately linearly for the proposed FRFP method. This also reflects in the experimental results shows in Fig. 14 and Fig. 16. Because the graphics processing unit (GPU) can rapidly manipulate and alter memory to accelerate the creation of images in a frame buffer intended for output to a display device, the calculation efficiency can be further improved by using GPU technology.

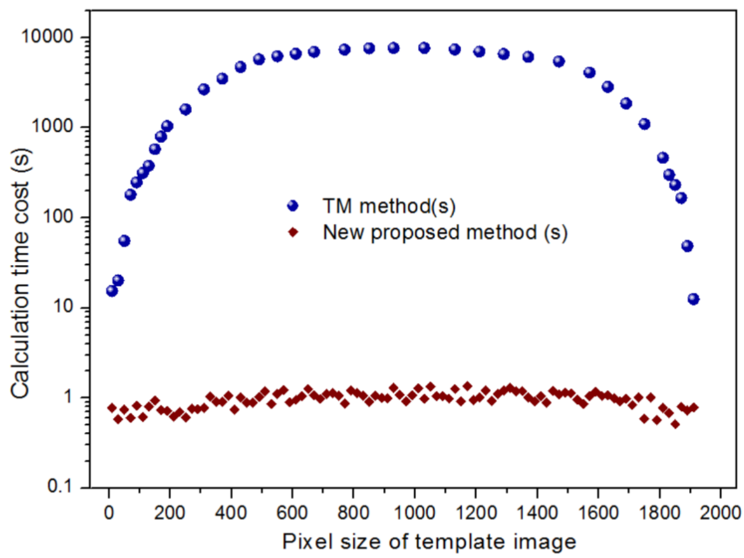

Fig. 16 Comparison between two algorithms in the case where the global image size is fixed.

3.4 Robustness

The robustness is another essential indicator to evaluate the performance of the algorithms. In the robustness experiment, the surface structure was measured using the Zygo Nexview 3D profiler as shown in Fig. 17. The experiment was divided into two parts. In the first part, an investigation about the change of scale and aspect ratio was conducted. In the second part, a study about the influence of noise was performed.

Fig. 17 Experimental setup of robustness test.

(1) Change of scale and aspect ratio

To test the robustness against the aspect ratio change, the experiment was divided into two groups from horizontal and vertical orientation respectively. Fig. 18 shows an example of a machining process with horizontal stretching noise. Compared with the original image in Fig. 18(a), there is no change in the pixel size along the vertical orientation, but the pixel size in the horizontal orientation reduces due to the horizontal stretching. Fig. 18(b) shows the matching results in the case of horizontal stretching, where the top left corner shows the partial enlargement. The results reveal that some groups of feature points can still be detected and then successfully matched. It indicates that the FRFP method is able to detect the aspect ratio change. The next step is to show the matching accuracy of the FRFP method under the aspect ratio change.

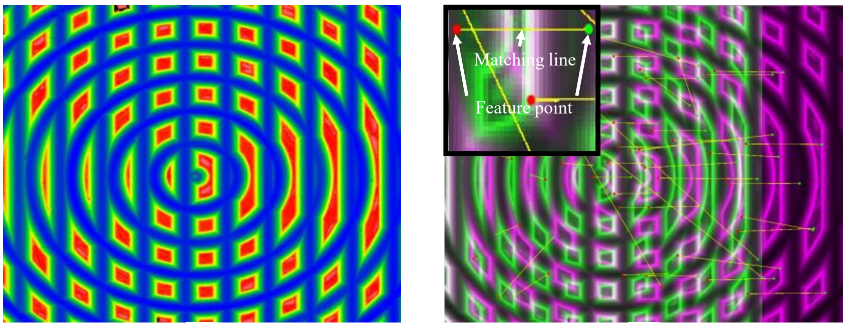

(a) (b)

Fig. 18 Matching process in the case of horizontal stretching: (a) image with horizontal stretching and (b) matching results.

The matching processes are conducted under different horizontal stretching ratios to test robustness performance. The results are shown in Fig. 19. Mathematically, the performance index of accuracy can be expressed as

$$Accuracy = 1 - \left| \frac{C_{rate} - R_{rate}}{R_{rate}} \right| \tag{9}$$

where C_{rate} refers to the calculated stretching rate and R_{rate} refers to the real stretching rate.

The results in Fig. 19 show that the accuracy is constant at 1 before the stretching rate increases to 1.18. After that, the accuracy starts to become unstable and fluctuant, and the overall trend is declining.

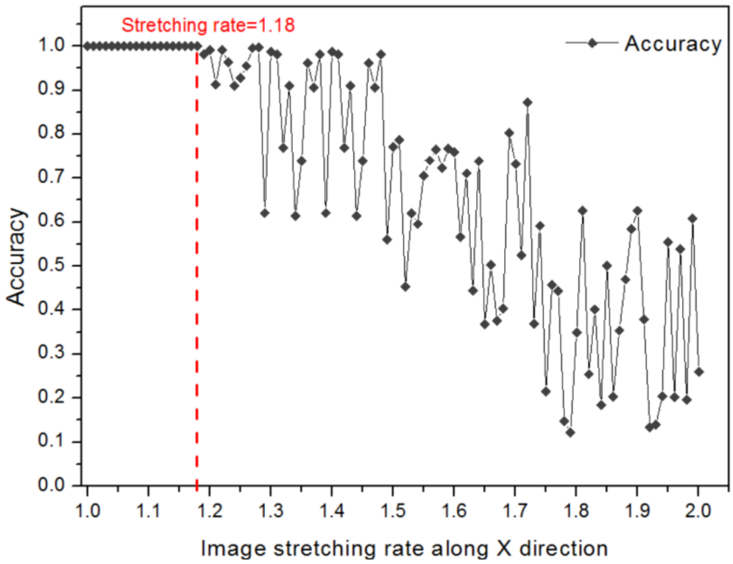

Fig. 19 Matching accuracy under different horizontal stretching ratios

In a similar manner, a control experiment was conducted in the case of horizontal stretching. An example of the matching process is shown in Fig. 20, and the results are shown in Fig. 21. The critical stretching rate point for this group is 1.14.

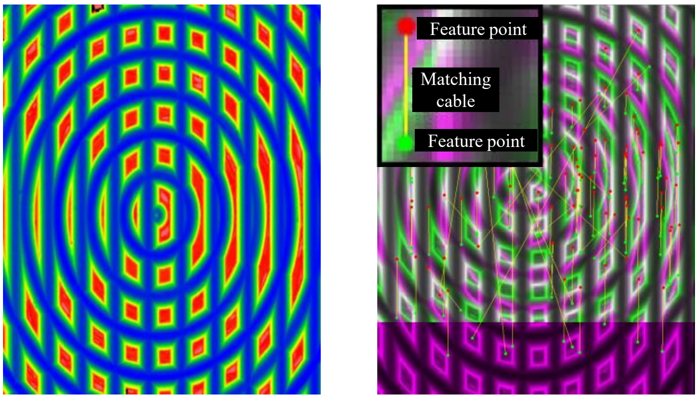

(a) (b)

Fig. 20 Matching process in the case of vertical stretching: (a) image with vertical stretching, (b) matching results.

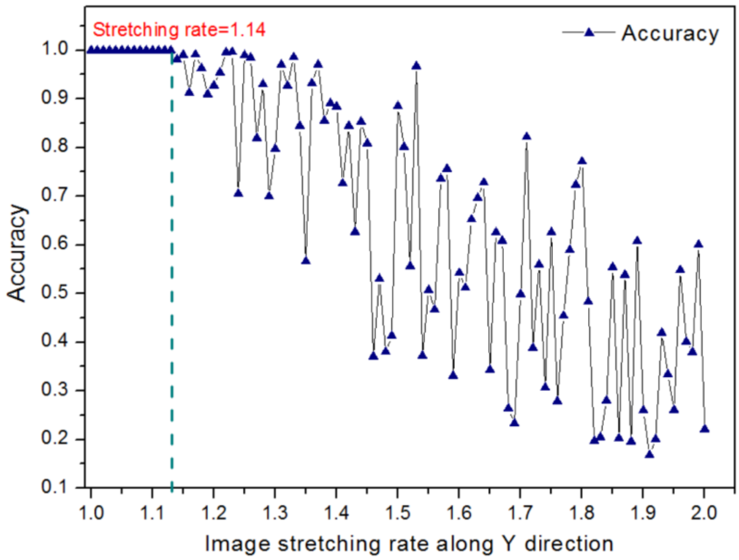

Fig. 21 Matching accuracy under different vertical stretching ratios.

It can be concluded that the FRFP method is able to resist an aspect ratio of no more than 1.14 both in the horizontal and vertical orientations. However, the noise of aspect ratio change is much less than 1.14 in most actual situations. As a result, the FRFP method has strong robustness to both scale and aspect ratio changes.

(2) Influence of noise

Noise is also one of the prime error sources. Here, some harsh noises that may occur in the real situation are specifically added to the images. The images with three typical noises, that is salt-and-pepper noise, speckle noise and Gaussian noise, are shown in Fig. 22. Salt-and-pepper noise, also known as impulse noise, is a form of noise sometimes seen on images, which can be caused by sharp and sudden disturbances in the image signal. It presents itself as sparsely occurring white and black pixels. Speckle noise is the grainy salt-and-pepper pattern present.

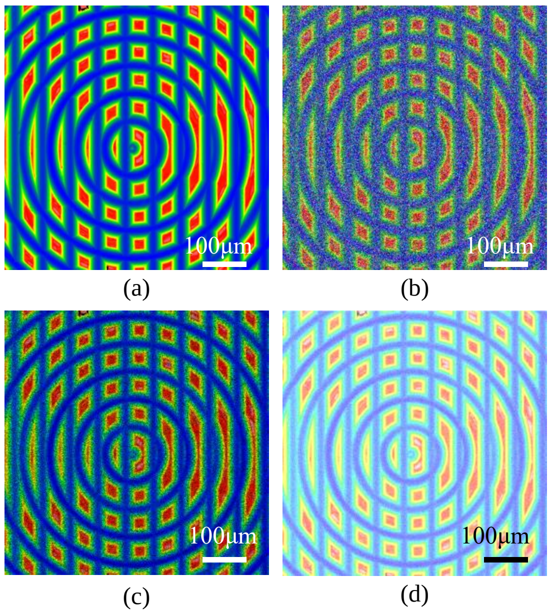

Fig. 22 Different types of noises (a) original image; (b) salt-and-pepper noise; (c) speckle noise; (d) Gaussian noise.

The experiments were conducted to investigate the matching accuracy of different areas of the polar microstructure. Gaussian noise as shown in Fig. 22(d) is the closest to the noise in actual situations because the values of the Gaussian noise can take on are Gaussian-distributed, which is closest to the real noise environment. Hence, it is chosen as the noise source in this experiment. Moreover, the noise intensity of Gaussian noise is set to be 0.15 which is far more than that in actual situations. As shown in Fig. 23, there are three representative areas which are the central area, horizontal area and vertical area. The matching process was conducted in the above different regions. The experimental results in Fig. 23(d) to Fig. 23(f) show that the FRFP method is also able to maintain high matching accuracy in different matching areas under the noise. As a result, the FRFP method has strong robustness to the noise.

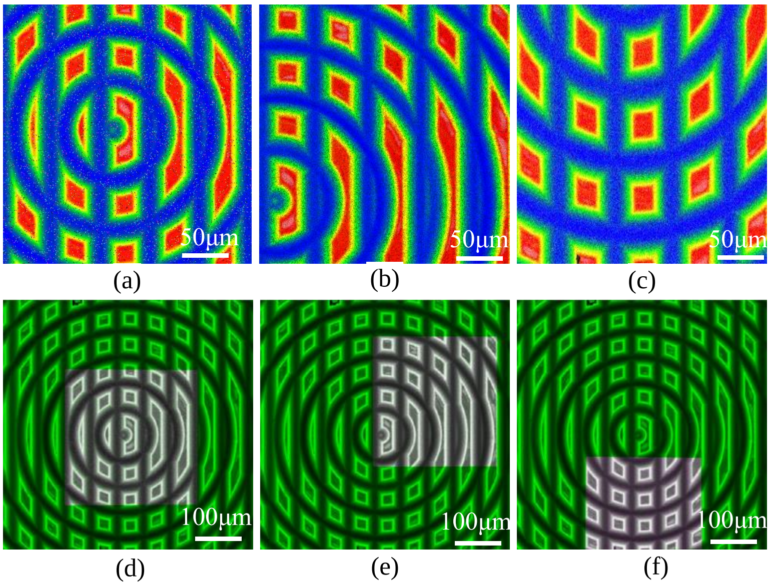

Fig. 23 Matching results for different areas of the polar microstructure under the noise (a) Central area (b) Horizontal area (c) Vertical area (d) Matching result of Fig. 23(a) (e) Matching result of Fig. 23(b) (f) Matching result of Fig. 23(c).

4 Conclusion

In this paper, the FRFP method is presented for optical nanoscale positioning. The relevant key algorithms are discussed. Different from the intensity-based TM method, the algorithms use feature-based points as the core to realize the matching. Concerning the concept of feature point, the algorithms consist of its detection, scale space building, localization, orientation assignment, descriptor generation, and matching. Theoretically, the FRFP method can realize the detection ability of angular/position displacement and improve the calculation speed and robustness. A series of experiments are conducted in these aspects to validate the actual performance. The experimental results show that it is able to detect angular displacement with a 100-arsecond-level measurement uncertainty. Compared with the TM method, the FRFP method improves various indicators for position displacement measurement uncertainty measurement. Most importantly, the FRFP method vastly improves the calculation speed by thousands of times. The robustness is also improved no matter whether the scale/aspect ratio change or the image noises. Overall, the FRFP method is proven to be capable of being used in future positioning measurements.

Reference

[1] Hack E, Burke J. Invited review article: measurement uncertainty of linear phase-stepping algorithms. Rev Sci Instrum 2011; 82(6): 061101.

[2] Chen M, Xie S, Zhou G, et al. Absolute distance measurement based on spectral interferometer using the effect of the FSR of a Fabry–Perot etalon. Opt Lasers Eng 2019; 123: 20-7.

[3] Yeh Y L, Wang C C, Jang M J, et al. A high-precision measurement technique for evaluating alcohol concentrations using an optical metrology system based on a position sensing detector. Opt Lasers Eng 2009; 47(5): 599-603.

[4] Gao W, Kim S W, Bosse H, et al. Measurement technologies for precision positioning. CIRP Ann-Manuf Technol 2015; 64(2): 773-96.

[5] Sommargren G E. A new laser measurement system for precision metrology. Precis Eng 1987; 9(4): 179-84.

[6] Song J H, Kim K C, Kim S H. Reducing tilt errors in moiré linear encoders using phase-modulated grating. Rev Sci Instrum 2000; 71(6): 2296-300.

[7] Villiger M, Braaf B, Lippok N, et al. Optic axis mapping with catheter-based polarization-sensitive optical coherence tomography. Optica 2018; 5(10): 1329-37.

[8] Orzechowski K, Sala-Tefelska M M, Sierakowski M W, et al. Optical properties of cubic blue phase liquid crystal in photonic microstructures. Opt Express 2019; 27(10): 14270-82.

[9] Binkele T, Hilbig D, Fleischmann F, et al. Using computer vision methods for the measurement of freeform surfaces with experimental ray tracing. In: 3D Image Acquisition and Display: Technology, Perception and Applications. Optical Society of America, 2018: JW4A. 23.

[10] Zhao C, Cheung C F, Liu M. Modeling and simulation of a machining process chain for the precision manufacture of polar microstructure. Micromachines 2017; 8(12): 345.

[11] Zhao C, Cheung C, Liu M. Integrated polar microstructure and template-matching method for optical position measurement. Opt Express 2018; 26(4): 4330-45.

[12] Zhao C, Cheung C F, Liu M. Nanoscale measurement with pattern recognition of an ultra-precision diamond machined polar microstructure. Precis Eng 2019; 56: 156-63.

[13] Williamson J, Martin H, Jiang X. High resolution position measurement from dispersed reference interferometry using template matching. Opt Express 2016, 24(9): 10103-14.

[14] Li H, Zhang X, Zhu B, et al. Micro-motion detection of the 3-DOF precision positioning stage based on iterative optimized template matching. Appl Opt 2017; 56(34): 9435-43.

[15] Trouvé E, Mauris G, Rudant J P, et al. Detection of linear features in synthetic-aperture radar images by use of the localized Radon transform and prior information. Appl Opt 2004; 43(2): 264-73.

[16] Yuan Y, Failmezger H, Rueda O M, et al. Quantitative image analysis of cellular heterogeneity in breast tumors complements genomic profiling. Sci Transl Med 2012; 4(157): 157ra143.

[17] Yoo J C, Han T H. Fast normalized cross-correlation. Circuits Syst Signal Process 2009, 28(6): 819.

[18] Goshtasby A A. 2-D and 3-D image registration: for medical, remote sensing, and industrial applications. John Wiley & Sons, 2005.

[19] Song Y, Chen Y H. Feature-based robot machining for rapid prototyping. Proc Inst Mech Eng Part B J Eng Manuf 1999; 213(5): 451-9.

[20] Yang Z Y, Chen Y H, Sze W S. Determining build orientation for layer-based machining. Int J Adv Manuf Technol 2001; 18(5): 313-22.

[21] Harris C G, Stephens M. A combined corner and edge detector. In: Alvey vision conference. 1988, pp. 10-5244.

[22] Lowe D G. Object recognition from local scale-invariant features. In: IEEE international conference on computer vision; 1999; p. 1150-7.

[23] Rosten E, Drummond T. Machine learning for high-speed corner detection. In: European conference on computer vision., Berlin Heidelberg, Germany: Springer; 2006. p. 430-43.

[24] Calonder M, Lepetit V, Strecha C, et al. Brief: Binary robust independent elementary features. In: European conference on computer vision. Berlin Heidelberg, Germany: Springer; 2010. p. 778–92.

[25] Rublee E, Rabaud V, Konolige K, et al. ORB: An efficient alternative to SIFT or SURF. In: International conference on computer vision 2011; p. 2564-71.

[26] Neubeck A, Van Gool L. Efficient non-maximum suppression. In: International Conference on Pattern Recognition 2006; p. 850-5.

[27] Stanković R S, Falkowski B J. The Haar wavelet transform: its status and achievements. Comput Electr Eng 2003; 29(1): 25-44.

[28] Wang L, Zhang Y, Feng J. On the Euclidean distance of images. IEEE Trans Pattern Anal Mach Intell 2005; 27(8): 1334-9.

[29] Tian Q, Huhns M N. Algorithms for subpixel registration. Comput Vis Graph Image Process 1986; 35(2): 220-33.